



MISR research-aerosol-algorithm refinements for dark water retrievals

J. A. Limbacher^{1,2} and R. A. Kahn¹

¹Earth Science Division, NASA Goddard Space Flight Center, Greenbelt, MD 20771, USA

²Science Systems and Applications Inc., Lanham, MD 20706, USA

Correspondence to: R. A. Kahn (ralph.kahn@nasa.gov)

Received: 19 May 2014 – Published in Atmos. Meas. Tech. Discuss.: 31 July 2014

Revised: 10 October 2014 – Accepted: 20 October 2014 – Published: 27 November 2014

Abstract. We explore systematically the cumulative effect of many assumptions made in the Multi-angle Imaging SpectroRadiometer (MISR) research aerosol retrieval algorithm with the aim of quantifying the main sources of uncertainty over ocean, and correcting them to the extent possible. A total of 1129 coincident, surface-based sun photometer spectral aerosol optical depth (AOD) measurements are used for validation. Based on comparisons between these data and our baseline case (similar to the MISR standard algorithm, but without the “modified linear mixing” approximation), for 558 nm AOD < 0.10, a high bias of 0.024 is reduced by about one-third when (1) ocean surface under-light is included and the assumed whitecap reflectance at 672 nm is increased, (2) physically based adjustments in particle microphysical properties and mixtures are made, (3) an adaptive pixel selection method is used, (4) spectral reflectance uncertainty is estimated from vicarious calibration, and (5) minor radiometric calibration changes are made for the 672 and 866 nm channels. Applying (6) more stringent cloud screening (setting the maximum fraction not-clear to 0.50) brings all median spectral biases to about 0.01. When all adjustments except more stringent cloud screening are applied, and a modified acceptance criterion is used, the Root-Mean-Square-Error (RMSE) decreases for all wavelengths by 8–27 % for the research algorithm relative to the baseline, and is 12–36 % lower than the RMSE for the Version 22 MISR standard algorithm (SA, with no adjustments applied). At 558 nm, 87 % of AOD data falls within the greater of 0.05 or 20 % of validation values; 62 % of the 446 nm AOD data, and > 68 % of 558, 672, and 866 nm AOD values fall within the greater of 0.03 or 10 %. For the Ångström exponent (ANG), 67 % of 1119 validation cases for AOD > 0.01 fall within 0.275 of the sun photometer

values, compared to 49 % for the SA. ANG RMSE decreases by 17 % compared to the SA, and the median absolute error drops by 36 %.

1 Introduction

The research aerosol retrieval algorithm has been a workhorse for analyzing and interpreting multi-angle, multi-spectral data from the NASA Earth Observing System’s Multi-angle Imaging SpectroRadiometer (MISR) instrument for over 15 years, and for investigating possible upgrades to the MISR operational aerosol algorithm (Kahn et al., 1998, 2001a). MISR was launched aboard the Terra satellite on 18 December 1999. The instrument measures upwelling shortwave radiance from Earth in four spectral bands centered at 446 (blue), 558 (green), 672 (red), and 866 nm (near-infrared, or NIR), at each of nine view angles spread out in the forward and aft directions along the flight path, at 70.5, 60.0, 45.6, 26.1°, and nadir (Diner et al., 1998). MISR has a swath width of roughly 380 km, and typically uploads data at a 1.1 km resolution (blue, green and NIR) for all channels (wavelengths and cameras), except for the 12 channels comprising the nadir camera and the red spectral band in the other eight cameras, which report data at a 275 m resolution. The instrument samples a very large range of scattering angles, with minimum scattering angle values of about 60° and maximum scattering angle values about 160° at mid latitudes, providing information about aerosol microphysical properties. These views also capture air-mass factors ranging from 1 to 3, offering sensitivity to optically thin aerosol layers, and allowing aerosol retrieval

algorithms to distinguish surface from atmospheric contributions to the top-of-atmosphere (TOA) radiance. For future reference, MISR aerosol “retrieval regions” are defined as the geographical areas over which aerosol retrievals are performed, which can be 16×16 , 4×4 , etc., 1.1 km image pixels. For the MISR Version 22 standard algorithm, retrievals are performed over 16×16 -pixel retrieval regions. In addition, we use “reflectance” to mean “equivalent reflectance” throughout the paper.

The research algorithm (RA) is designed to provide flexibility in selecting (1) retrieval region spatial resolution, (2) aerosol optical models (mixtures) to be included in the algorithm comparison-space aerosol climatology, and (3) acceptance criteria for retrieved aerosol amount and type, at the expense of the speed and autonomy required of the MISR Standard Operational algorithm (SA). As such, we can perform case studies and analyses over selected areas, but it is not feasible to generate global products with this algorithm. Early versions of the RA could analyze only single retrieval regions at a time (assessed over any number of chosen pixels), and could simulate only dark water surfaces of varying wind speed. Making use of recent advances in computer hardware and software technology, the MISR RA has been modified so it is practical to obtain results simultaneously for a number of retrieval regions within a geographic domain, while retaining flexibility in aerosol type and acceptance criteria options (e.g., Kahn and Limbacher, 2012).

This paper reports on upgrades to the MISR research aerosol retrieval algorithm as they affect dark water retrievals. The changes are motivated in part to explore issues identified in recent validation analysis performed on the MISR Standard aerosol product (Kahn et al., 2010). The validation study showed, for example, that at low AOD the V22 Standard product AOD tends to be overestimated, whereas at high AOD, the very limited number of over-ocean validation cases suggest the V22 product might be underestimated, relative to near-simultaneous surface-based sun photometer measurements. In the current paper, we examine in detail the quantitative effect of specific upgrades to the research algorithm on retrieved AOD and Ångström Exponent (ANG). We implement and assess even minor adjustments that are justified on physical grounds, such as recent refinements to ocean surface whitecap spectral reflectivity and atmospheric gas spectral absorption parameters, with the understanding that the cumulative effects of even small corrections can be significant. Section 2 describes the latest implementation of the MISR dark water approach in the RA. Section 3 describes various modifications that are made to the algorithm based on theoretical or physical considerations. Section 4 describes empirical adjustments that are made to the algorithm, as well as AOD validation, ANG validation, and the effects of more stringent cloud screening. Conclusions are presented in Sect. 5.

2 MISR research retrieval dark water algorithm, and validation data

The essential aspects of the MISR Standard dark water retrieval algorithm are given in Martonchik et al. (1998, 2002) and Diner et al. (2008), and are similar to the historical implementation in the research algorithm (Kahn et al., 1998, 2001a). A flowchart outlining the steps involved in the aerosol retrieval over dark water for the research algorithm is presented in Fig. 1. For the current implementation of the algorithm, the dark water portion of the code is run if the SA performs a dark water retrieval and the sub-region used has the MISR SA product variable `SurfaceFeatureID` ≥ 5 (indicating, dark water). The most recent applications of the RA are closest to the SA version presented by Diner et al. (2008), with differences and new modifications as indicated below (differences between the baseline RA and the SA are minor). Pre-processing of the MISR radiances in the RA includes converting radiance to equivalent reflectance, performing out-of-band spectral corrections, and making ozone, water vapor, and atmospheric gas polarization corrections as described in Kahn et al. (2001b, 2007), with minor net atmospheric gas optical depth increases compared to previous implementations of 0.0002 (blue), 0.0008 (green and red), and 0.0025 (NIR) based on refinements to the O_3 and H_2O_v spectra (<http://spectralcalc.com>).

2.1 Retrieval algorithm setup

For the baseline version of the RA we represent the ocean surface as is done in the SA, with standard, wind-driven, isotropic surface roughness (i.e., Cox–Munk, independent of wind direction) and whitecap models, a glint exclusion angular region of about 40° around the specular direction, and an otherwise black surface in the MISR red and NIR bands at all viewing angles (e.g., Martonchik et al., 1998).

Initial comparisons of MISR coincidences with the AEROSOL ROBOTIC NETWORK (AERONET) (Holben et al., 1998) and Marine Aerosol Network (MAN; Smirnov et al., 2009) surface-based sun photometer data indicates a high bias in MISR AOD when the total-column, mid-visible (green) AOD falls below about 0.4 (Kahn et al., 2005b, 2010; Witek et al., 2013). This bias is present in both the SA and RA, although the greater variety of mixtures in the RA appears to mitigate the bias in some cases. Four main factors can contribute to this issue: (1) instrument radiometric calibration, (2) the angularly dependent ocean surface reflectance (the bi-directional reflectance distribution function or BRDF), (3) the aerosol type and vertical distribution that define the aerosol optical model adopted in the retrieval, and (4) cloud contamination. The magnitudes of the contributions from these factors are expected to vary systematically with wavelength, view angle, and environmental conditions, in ways that can help identify causes. For example, ocean color will have a larger impact at shorter wavelengths and

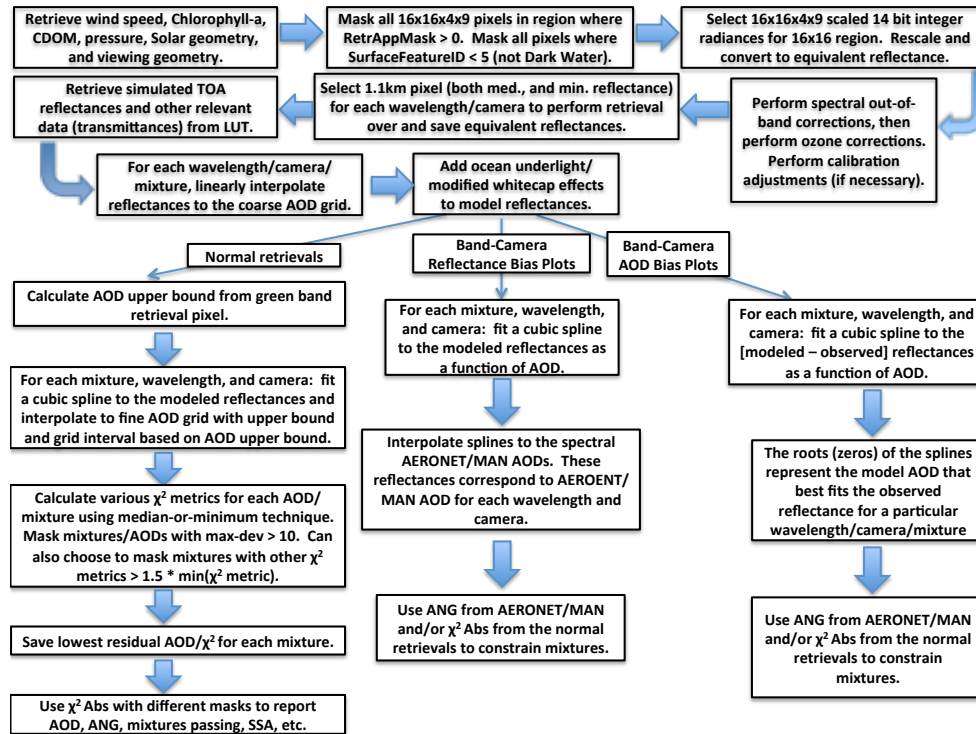


Figure 1. Flow chart summarizing the steps involved in research algorithm aerosol retrievals over dark water.

near-nadir view angles, whereas the aerosol optical model is more likely to dominate at steeper view angles and higher AOD, and will depend on the dominant aerosol type in a given region.

The wind speeds used in the RA previously came from the SfcWindsp data set found in the MISR SA aerosol files, which are obtained from monthly satellite scatterometer data (Quikscat until November 2009), then SSM/I imager data (Diner et al., 2008; Kahn et al., 2009a; C. Moroney, personal communication, 2014). Because wind speed can vary considerably during a month, we use here the Cross-Calibrated Multi-Platform (CCMP) wind data specific to within 6 h of the MISR observation (Atlas et al., 2011). The CCMP data sets include scatterometer data and microwave imaging data, which are then merged with ocean buoy data and reanalysis data via a Variational Analysis Method. This merged data set produces Root-Mean-Square-Error (RMSE) errors of 1.6 m s^{-1} relative to ship observations, on a grid of 0.25° resolution. Because this data is only available through the end of 2011 (and from 78° S to 78° N), we use the MISR SA winds when and where CCMP data are unavailable.

When applying the RA, the radiative transfer code is run for an eight-dimensional space, covering ranges of viewing and solar geometry, AOD and aerosol mixture type, spectral band, surface atmospheric pressure, and for over-ocean retrievals, wind speed (Table 1). As with the SA, the radiative transfer result is referred to as the Simulated MISR Atmospheric Radiative Transfer (SMART) array (Diner et

al., 2008). For a given retrieval, for each camera, values for the solar geometry, surface atmospheric pressure, and wind speed are linearly interpolated within the SMART array to the values appropriate to that case, reducing the dimensionality of the remaining space to four (mixture, AOD, spectral band, and camera). With the implementation of the RA used here, the AOD grid in the SMART array, which is at a coarse resolution (Table 1), is then interpolated using a cubic spline for each mixture, camera, and band, to produce simulated TOA reflectances on an adaptive mid-visible AOD grid of finer resolution.

The minimum AOD value for the adaptive grid is set to 0.0. To determine the maximum AOD value, first the largest possible AOD is estimated from the observed green-band TOA reflectances, separately for each aerosol mixture and each camera used, assuming the surface is dark water. To obtain the maximum green-band AOD for the retrieval overall, the smallest maximum AOD among the cameras is selected for each mixture, and then the maximum of these among all mixtures is the final choice. This process allows us to reduce processing time and perform retrievals with more precision, while still retaining a liberal maximum allowed value for the AOD. AOD maxima in the other spectral bands are determined from the ratios of the spectral extinction cross-sections for each mixture.

With the minimum and maximum AOD established from the coarse SMART array, cubic splines are used to generate the finer grid in the AOD dimension for each aerosol mixture,

Table 1. Dimensions of the MISR RA look-up table (LUT), representing the SMART output.

Variable	Description	Values
μ_0	Cos (sun zenith angle)	0.2–0.9 (in 0.05 increments); 0.925, 0.95, 0.975, 0.99, 1.0
μ	Cos (view zenith angle)	0.31, 0.33, 0.35; 0.47, 0.49, 0.51; 0.66, 0.685, 0.71; 0.84, 0.87, 0.9; 0.95, 0.975, 0.99, 1.0
τ	Spectral AOD	0, 0.05, 0.1, 0.2, 0.35, 0.55, 0.75, 1.0, 1.5, 2, 3, 5, 7, 9.5
P	Surf. Pressure (mb)	607.95, 1050.0
u	Surf. Wind Speed (m s^{-1})	0.5, 5.0, 7.5, 10.0, 12.5
λ	Spectral Band (nm)	446 (blue), 558 (green), 672 (red), 866 (NIR)
Θ^*	Scattering Angle	0.0 (minimum) – 180.0 (maximum). Scattering angle range varies based on μ_0, μ .
m	Aerosol Mixture	74 Kahn et al. (2010) or 774 [Tables 3 and 4]

* Scattering Angle grids (a grid for each $\mu - \mu_0$ combination) were selected so maximum errors in the interpolated LUT values do not exceed 1 % of the value compared to a 1° resolution scattering angle grid. For view zenith angle, triplets allow for changes in viewing zenith in the across-track direction. View zenith angle changes by about 17° across-track for the nadir camera.

camera, and band. If the maximum green-band AOD for the retrieval is below 0.15, we interpolate to a fine-grid spacing of ~ 0.001 to achieve maximum AOD sensitivity; for AOD between 0.15 and 1.0, we interpolate to 0.002, and at higher maximum AOD, we use a grid of 0.005. Then the minima of a set of χ^2 test variables are assessed on this fine AOD grid for the AOD retrieval, separately for each mixture.

The χ^2 test variables are described in detail in previous papers (e.g., Kahn et al., 1998; Kahn and Limbacher, 2012). Briefly, the absolute χ^2 variable (χ_{abs}^2) is defined as follows:

$$\chi_{\text{abs}}^2 [\text{mix}, \text{AOD}] = \frac{\sum_{\lambda, c} w \frac{(\rho - \rho_{\text{mod}})^2}{\rho_{\text{err}}^2}}{\sum_{\lambda, c} w}. \quad (1)$$

The band and camera weights are represented by $w(\lambda, c)$, and are currently set to μ^{-1} , where μ is the cosine of the view angle, λ is the wavelength index, c is the camera index, ρ is the TOA observed reflectance, ρ_{mod} is the TOA modeled reflectance, mix is the aerosol mixture, AOD is the AOD at which ρ_{mod} is assessed, and ρ_{err} is the total estimated uncertainty of the model/measurements (taken nominally as 5 % of the observed spectral reflectance value or 0.002, whichever is larger, but see Sect. 3.4 below). For each particular AOD and mixture, the χ^2 value is computed by performing the summation over all wavelengths and cameras used for the retrieval.

In addition to χ_{abs}^2 , we also obtain the maximum deviation test variable, χ_{maxdev}^2 , defined as follows:

$$\chi_{\text{maxdev}}^2 [\text{mix}, \text{AOD}] = \max \left(\frac{(\rho - \rho_{\text{mod}})^2}{\rho_{\text{err}}^2} \right). \quad (2)$$

Note that the maximum deviation is assessed over all wavelengths and cameras used in the aerosol retrieval, such that there is one χ_{maxdev}^2 value for each mixture and AOD. Note also that over ocean, acceptance criteria for aerosol mixtures and AOD values are applied for the MISR red and NIR bands only, to minimize uncertainties based on the

ocean surface modeling and other factors, such as sensitivity to polarization and aerosol vertical distribution. The green and blue values are calculated for all cases anyway, so we can assess the information content of the observations and the validity of optical properties reported for those bands. Only cameras for which the MISR SA Retrieval Applicability Mask (RetrAppMask) quality flag is 0, the glitter angle exceeds 40° , and the subregion is identified as being either inland water or deep ocean, are used for calculating the χ^2 metrics; mask values greater than 0 imply that glint, cloud, or cloud shadow could be issues (e.g., Kahn et al., 2009b).

Any mixture/AOD combination having $\chi_{\text{maxdev}}^2 > 10$ is eliminated from further consideration. We then take the AOD corresponding to the minimum χ_{abs}^2 for each mixture, such that if the algorithm climatology contains 74 mixtures, we save 74 χ_{abs}^2 values and their corresponding AODs. We then use χ_{abs}^2 to constrain AOD over ocean, and unless specified otherwise, a χ_{abs}^2 criterion is applied for the figures and results in this paper. For example, we accept all (mixture, AOD) pairs for which the residuals between the calculated and observed TOA equivalent reflectances fall within $1.5 \times \text{chiMin}$ of χ_{abs}^2 , where chiMin is the lowest value among all mixtures and AOD values in the algorithm climatology. Other acceptance criteria are discussed subsequently, as needed.

For the purpose of identifying possible camera or spectral-band-specific biases, we also save the AOD that corresponds to a residual ([model – observed reflectance]) value of 0.0 for each camera, band, and aerosol mixture. In general, the minimum absolute residual should be 0.0, unless the actual surface is much brighter than expected, or if the aerosol optical model is grossly incorrect. These AOD values correspond to the roots (zeros) of spline fits to the residuals on the coarse optical depth grid (defined in Table 1), specific to each camera, band, and mixture. We can then use constraints on aerosol type from the χ^2 tests, and by comparison with ANG values from coincident AERONET or MAN observations, to assess the individual camera and spectral band biases.

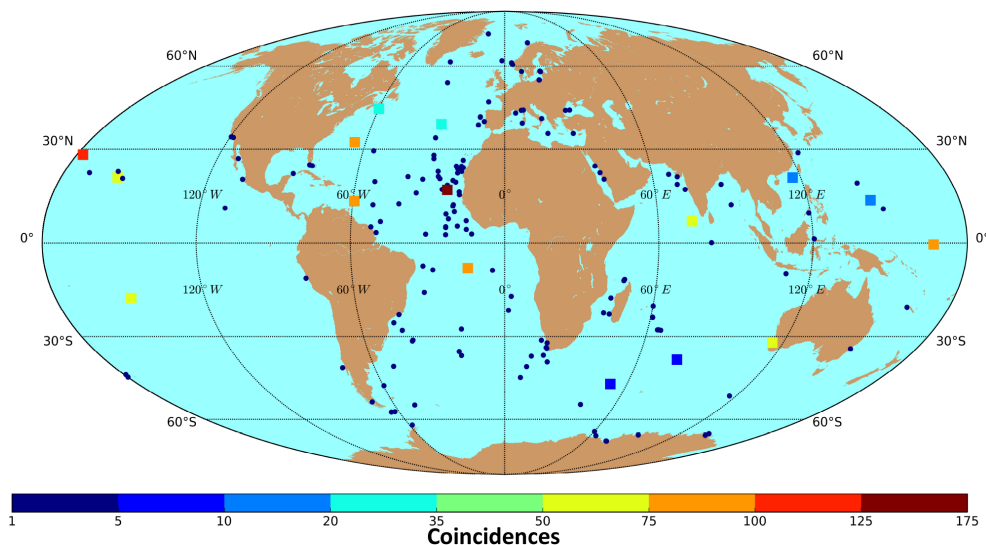


Figure 2. Map showing the geographical distribution of 951 MISR-AERONET and 178 MISR-MAN validation cases. Squares are used for AERONET sites and circles for MAN. Symbol color indicates the number of coincidences for each MAN/AERONET site.

Our analysis approach uses coincident spectral AOD measurements from the AERONET (Holben et al., 1998) and MAN (Smirnov et al., 2009) sun photometer data sets for validation, interpolated to the MISR wavelengths, as in earlier work (e.g., Kahn et al., 2010). The RA code is run with varying assumptions and constraints, and the residuals are calculated for the validation cases, independently for each band and camera. As a partial test of MISR-retrieved aerosol properties, we can also filter the data, keeping for example only those MISR-retrieved mixtures having Ångström exponents within 0.10 of the corresponding MAN/AERONET ANG derived from the interpolated MAN/AERONET AODs. Such constraints are available only at sun photometer sites; the cases rejected by this test highlight situations where providing external particle property information or assumptions would have the biggest impact on MISR retrieval quality.

2.2 MAN/AERONET-MISR data selection

For the present study, we use AERONET level 2.0 data (cloud-screened (Smirnov et al., 2000) and quality assured) that is spatially coincident with at least one region in a 3×3 MISR Standard retrieval region (each of which is 17.6 km in horizontal extent) and within ± 1 h of the MISR overpass (Holben et al., 2006). For MAN data, we use ± 30 min for the temporal constraint, due to generally greater temporal variability (ships move whereas AERONET sites do not, and the platform is generally less stable). The sun photometer data are then averaged over this window and interpolated to the four MISR wavelengths using a 2nd-order polynomial fit in log space. Additionally, for AERONET data we add the constraint that there be at least one AOD measurement on each side of the 1-hour time window. For the entirety of this pa-

per, we consider only dark-water MISR retrievals. The specific AERONET sites chosen were selected for consistency with previous work (Kahn et al., 2010), and to ensure that artifacts due to runoff, aerosol heterogeneity, and under-light are minimized.

Figure 2 shows the geographic distribution of the MAN/AERONET-MISR coincidences used for the current study. Our validation data set includes only island AERONET sites (951 cases) plus 178 ship-based MAN cases, because the surfaces at these sites tend to be less polluted with run-off or biological activity than the more abundant AERONET coastal sites. Additionally, assuming that island sites are less likely to be major aerosol sources, the retrieved aerosol amount and type should be more homogeneous over a 3×3 retrieval-region area than at coastal sites. Table 2 lists the number of MISR-AERONET collocations based on site location. Using the MISR SA RetrAppMask quality flag (containing [16×16 pixels \times 4 MISR bands \times # of cameras used] elements per retrieval), we designate a region as “clear” (a value of 0) if the mask identifies less than x % of the region as having a flag value greater than 0, where x can be specified; for example, we could require at least 50 % of pixels to pass all the radiance acceptance tests (e.g., Kahn et al., 2009b), not counting those cameras entirely eliminated from consideration due to glint. Because we can remove glint-contaminated cameras prior to running the RA, these flagged values should correspond primarily to clouds or cloud shadows (via the MISR SA brightness, direct cloud, angular smoothness or angular correlation masks, Martonchik et al., 2002). The RA ingests relevant ocean color data from the GlobColour group (Barrot et al., 2010), which merges spatially coincident data from the Moderate Resolution Imaging Spectroradiometer (MODIS)-

Table 2. Number of MISR-AERONET coincidences

Site Name	Coincidences
Amsterdam Island	8
Ascension Island	75
Azores	25
Bermuda	34
Capo Verde	167
Crozet Island	9
Dongsha Island	15
Guam	15
Lanai	66
MCO-Hanimaadhoo	57
Midway Island	109
Nauru	88
Ragged Point	90
Rottneest Island	54
Sable Island	25
Tahiti	56
Tudor Hill	58
Total	951

Aqua, the Sea-Viewing Wide Field-of-View Sensor (SeaWiFS), and the Medium Resolution Imaging Spectrometer (MERIS), using the Garver–Siegel–Maritorena (GSM) model (Maritorena and Siegel, 2005). The data shown in Table 2 and Fig. 2 include all MISR-MAN/AERONET coincidences used in this study for which the MISR SA and MISR RA provide at least one (coincident) dark-water retrieval.

2.3 The baseline case

We consider the data used to generate Figs. 3 and 4 to be the baseline cases, against which all other retrieval experiments are compared. The data shown in these two figures were generated with the 74 aerosol-mixture climatology used in Version 22 of the SA (Kahn et al., 2010). The main difference between the SA and the RA as applied for Figs. 3 and 4 is that the modified linear mixing approximation (Abdou et al., 1997) is not used in the RA; instead, the full radiative transfer code is run for each mixture (see Sect. 3.3.2 below).

Figure 3 shows the MISR RA AOD bias relative to the sun photometer values, for each spectral band and camera, for all AERONET/MAN data. Note that the red-channel retrieved AOD has a small high bias in AOD for most cameras (>0.01), whereas the NIR band has a smaller high bias in AOD (~ 0.01). The blue is biased high by >0.20 for all cameras, and the green is biased high by >0.05 for most cameras.

Figure 4 and Table 3 show the MISR research retrieval AOD results compared to AERONET/MAN for the baseline case at all four wavelengths. Note that $>70\%$ of the RA results, using the 74-aerosol-mixture climatology of the SA but without the modified linear mixing approximation, fall within the greater of 0.05 or 20% for all wavelengths, and

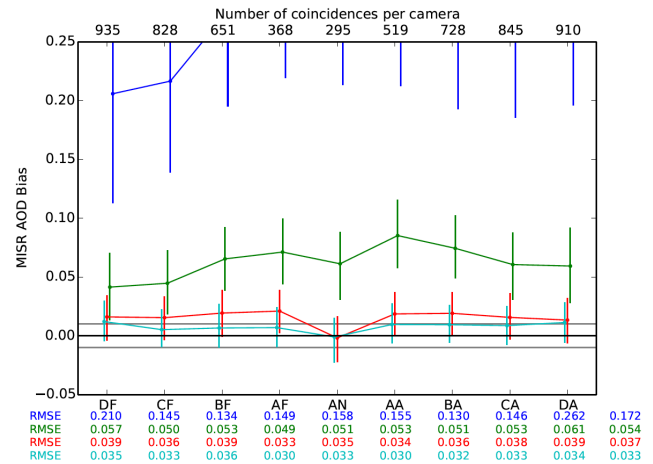


Figure 3. RA baseline case bias plots. The plot shows the aggregated AOD bias in each MISR channel (calculated according to the rightmost branch of Fig. 1), when all the validation data used in the study are included. The points represent the median values for each particular wavelength and camera; the vertical bars represent the 25th–75th percentiles. The count is shown for each camera near the top of the plot, and the RMSE (for each camera and spectral band) is shown near the bottom, color-coded by spectral band. The numbers on the bottom right give the camera-averaged values for the RMSE. Median values in the blue band are off-scale for nearly all cameras. The grey horizontal lines are centered on ± 0.01 , for reference. The overall statistics for each spectral band (following the left branch of Fig. 1) are given as the “RA Baseline” entries in Table 3.

$>80\%$ for all but the blue band. This is comparable to ($\sim 5\%$ better than) the result for a broader set of Maritime cases assessed with the SA by Kahn et al. (2010). The results (both ANG and spectral AOD) for the SA are also shown in Table 3 and in the summary figures of Sect. 4.

3 Algorithm modifications based on physical considerations

This section describes the impact on retrieved AOD of individual modifications to the way (1) observed reflectances over a retrieval region are selected, (2) the ocean surface is modeled, (3) the aerosol components and mixtures are defined, and (4) the measurement uncertainty is assessed in the calculation of the retrieval acceptance test variables. These changes are motivated by physical considerations described in each subsection.

3.1 Selection of TOA reflectances

When comparing with SA results over ocean, we select for the nominal RA case the same MISR reflectances as used by the SA, i.e., for each 1.1 km pixel within the retrieval region that passes the SA cloud contamination, shallow water, and other tests (Kahn et al., 2009b), the reflectances in the red

Table 3. Statistics of AOD and ANG retrievals stratified by adjustment*.

Adjustment	0.05 or 20 %	0.03 or 10 %	SD	RMSE	MAE	Med Bias	#
SA	62	38	0.059	0.073	0.042	0.038	1123
SA + 0.5 FNC	68	43	0.054	0.065	0.036	0.032	982
RA Baseline	70	44	0.058	0.064	0.036	0.027	1129
RA + Median or Min	73	47	0.055	0.060	0.034	0.024	1129
RA + Ocean Surface	78	53	0.056	0.058	0.029	0.016	1129
RA + Mixtures	79	53	0.051	0.054	0.030	0.019	1129
RA + All Adj.	84	62	0.047	0.047	0.024	0.010	1123
RA + All Adj. + 0.5 FNC	88	67	0.044	0.044	0.021	0.005	982
Adjustment	0.05 or 20 %	0.03 or 10 %	SD	RMSE	MAE	Med Bias	#
SA	76	52	0.048	0.056	0.030	0.026	1123
SA + 0.5 FNC	81	60	0.043	0.048	0.025	0.020	982
RA Baseline	81	56	0.046	0.050	0.027	0.020	1129
RA + Median or Min	84	58	0.043	0.046	0.026	0.017	1129
RA + Ocean Surface	85	61	0.045	0.047	0.024	0.015	1129
RA + Mixtures	84	61	0.043	0.046	0.025	0.017	1129
RA + All Adj.	87	68	0.039	0.040	0.021	0.010	1123
RA + All Adj. + 0.5 FNC	91	74	0.036	0.037	0.018	0.006	982
Adjustment	0.05 or 20 %	0.03 or 10 %	SD	RMSE	MAE	Med Bias	#
SA	83	63	0.041	0.047	0.023	0.019	1123
SA + 0.5 FNC	88	69	0.036	0.039	0.020	0.012	982
RA Baseline	86	64	0.039	0.043	0.023	0.016	1129
RA + Median or Min	88	66	0.037	0.039	0.021	0.013	1129
RA + Ocean Surface	86	66	0.039	0.042	0.021	0.014	1129
RA + Mixtures	86	65	0.039	0.042	0.022	0.016	1129
RA + All Adj.	89	72	0.036	0.037	0.019	0.010	1123
RA + All Adj. + 0.5 FNC	92	78	0.032	0.032	0.016	0.006	982
Adjustment (NIR)	0.05 or 20 %	0.03 or 10 %	SD	RMSE	MAE	Med Bias	#
SA	88	70	0.037	0.040	0.019	0.013	1123
SA + 0.5 FNC	92	77	0.032	0.033	0.016	0.007	982
RA Baseline	88	69	0.035	0.038	0.019	0.012	1129
RA + Median or Min	89	71	0.033	0.035	0.018	0.010	1129
RA + Ocean Surface	87	67	0.035	0.039	0.020	0.014	1129
RA + Mixtures	87	67	0.036	0.040	0.020	0.016	1129
RA + All Adj.	91	74	0.033	0.035	0.018	0.010	1123
RA + All Adj. + 0.5 FNC	94	79	0.029	0.029	0.015	0.005	982
Adjustment (ANG)	0.5	0.275	SD	RMSE	MAE	Med Bias	#
SA	78	49	0.399	0.450	0.279	0.215	1119
SA + 0.5 FNC	76	47	0.386	0.454	0.296	0.237	976
RA Baseline	79	55	0.455	0.463	0.246	0.060	1125
RA + Median or Min	78	53	0.463	0.473	0.258	0.070	1125
RA + Ocean Surface	82	59	0.421	0.431	0.214	-0.071	1125
RA + Mixtures	87	65	0.383	0.386	0.185	-0.035	1125
RA + All Adj.	88	67	0.364	0.374	0.179	-0.051	1119
RA + All Adj. + 0.5 FNC	88	67	0.352	0.359	0.183	-0.042	979

* Columns 2 and 3 give the percent of validation cases within the confidence envelopes indicated, SD is the standard deviation, RMSE is the root-mean-square error, MAE is the mean absolute error, Med Bias is the median bias, and # is the number of validation cases included. The first four data blocks give the spectral AOD statistics, and the fifth data block presents the ANG statistics. Bolding highlights the key results.

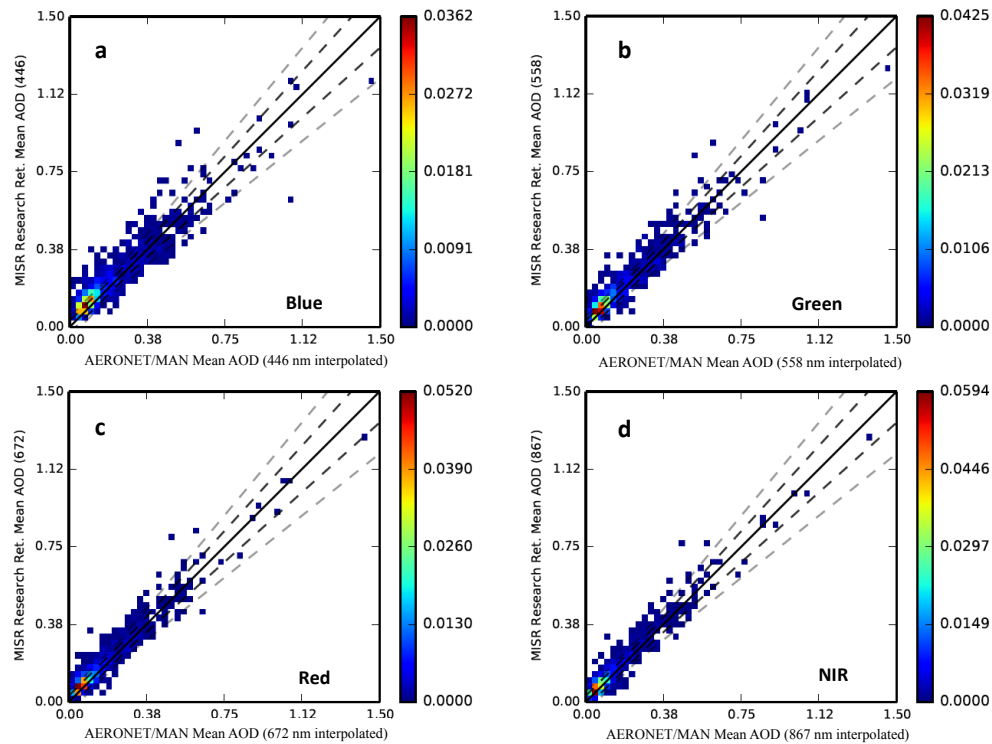


Figure 4. RA baseline case scatter-density plots. The color scale to the right of each plot represents the fractional density of data. These panels present the joint PDF of MISR-AERONET/MAN data for the four MISR spectral bands: (a) Blue, (b) Green, (c) Red, (d) NIR.

and NIR bands for all available cameras are averaged with equal weight, and the darkest pixel is taken as representing the 16×16 pixel retrieval region. As such, red band contributions generally dominate over dark water, because dark water tends to be brighter at shorter wavelengths. However, at other times we adopt alternative strategies for the RA, such as (1) taking the darkest pixel channel-by-channel, or (2) making a selection based on the histogram of reflectances over the useable pixels in the entire retrieval region, as is done for MODIS (e.g., Remer et al., 2005). We also examined an approach that takes account of scene attributes that vary with AOD and cloud fraction.

When scene variability is dominated by something other than aerosol, i.e., at low AOD or high fraction not-clear (FNC), the retrieval is more likely to contain surface or cloud artifacts, respectively, that can increase the observed TOA reflectance. So for this experiment, if green band AOD < 0.35 (based on the darkest pixel) or FNC ≥ 0.10 for the region, we select the minimum reflectance pixel over the retrieval region, independently for each spectral band and camera, under the assumption that the aerosol is uniform over the region.

At higher AOD, aerosol variability is likely to become important, so the darkest pixel might not best represent retrieval-region reflectance as a whole, especially if, at the same time, FNC is very low. So if the green band AOD ≥ 0.35 (determined by using the minimum reflectance pixel with the traditional χ_{abs}^2 metric) and FNC ≤ 0.10 for

the region, we select the median reflectance pixel over the retrieval region, independently for each spectral band and camera. If $0.0 < \text{FNC} < 0.10$, we take a linear weighting of the median reflectance pixel and the minimum reflectance pixel. So, for example, at FNC of 0.025, the total reflectance would be the sum of 25 % of the minimum reflectance pixel plus 75 % of the median reflectance pixel.

The scatter-density plot for the RA when this “median-or-minimum” approach is applied looks very similar to the baseline case of Fig. 4 and is not shown, but the quantitative differences are given in Table 3. The alternative pixel selection incrementally reduces the retrieved AOD root mean square error (RMSE) by 5–10 %, the median bias decreases by 10–20 % in all bands, and there are fewer outliers for these cases.

3.2 Ocean surface model

In a previous study, the RA considered an isotropic (Lambertian) component of the reflection from within the water (“under-light”), using spectrally dependent albedo values from ocean surface observations available at the time (Kahn et al., 2005a). Here we expand on previous work by accounting for the two dynamic components of under-light (along with surface whitecaps), as discussed in Sayer et al. (2010). We consider this ocean surface model as a limiting case, to explore the degree to which the factors involved might

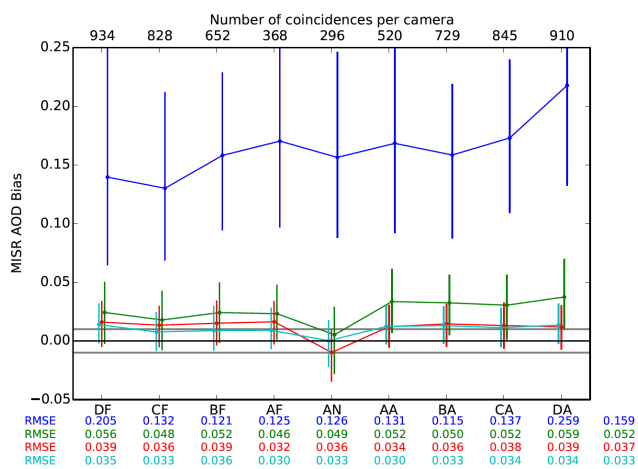


Figure 5. Channel-by-channel MISR AOD biases including all validation data, similar to Fig. 3, but when the under-light and modified whitecap representations are applied to the RA baseline algorithm. The overall statistics for each spectral band are given as the “RA + Ocean Surface” entries in Table 3.

affect AOD retrieval quality. Contributions to the changing under-light can come from (1) colored dissolved organic matter and detrital organic materials absorption (CDOM) and (2) Chlorophyll *a* (C). We use the GlobColour GSM monthly ocean color products (Barrot et al., 2010), taking the high-resolution (4.4 km) C and CDOM values nearest to the center of the MISR retrieval region. Information on the uncertainty of the C and CDOM data sets can be found in Maritorena et al. (2010). If the region has no valid monthly values for either C or CDOM, we use default values of $\sim 0.01 \text{ m}^{-1}$ (558 nm) for the CDOM absorption coefficient and 0.20 for the Chlorophyll *a* concentration. The contribution of water molecular scattering is included in the under-light model (details can be found in Sayer et al., 2010). Recent measurements also report on the angular dependence of the ocean surface reflectance (e.g., Voss and Chapin, 2005; Antoine et al., 2013). However, it is not clear how general these results might be, so including this refinement is beyond the scope of the current study; having additional constraints on ocean surface BRDF would be an asset to multi-angle remote sensing of Earth’s surface.

The whitecap model used by the current standard and baseline research algorithms assumes a spectrally invariant effective whitecap albedo of 0.22 from Koepke (1984), with wind-speed-dependent whitecap coverage from Monahan and O’Muircheartaigh (1980). We adopt alternative albedo values of 0.40 for the blue and green, 0.36 for red, and 0.24 for NIR, based on Frouin et al. (1996) and consistent with Sayer et al. (2010).

In Fig. 5 we show the updated channel-by-channel biases when we account for under-light and the updated effective whitecap albedo, when the retrieved aerosol mixture is the same for all channels, but the AODs are retrieved for each

band and camera separately (Fig. 1, rightmost branch). The AOD bias in the blue and green drops substantially when under-light and updated whitecaps are included, compared to the baseline case shown in Fig. 3; blue bias decreases by ~ 0.1 , though it is still ~ 0.15 , and green decreases by > 0.03 . The AOD bias in the red drops by a much smaller absolute amount (< 0.004), and the NIR increases slightly (< 0.004). The slight NIR increase is due to changes between Figs. 3 and 5 in the mixtures selected (the retrieved particle size increases, retrieved ANG decreases). If the mixtures chosen for the ocean-surface-model retrievals were identical to the baseline case, the red AOD bias would decrease by ~ 0.007 and the NIR would decrease by ~ 0.0007 . Also, because we do not use either the blue or green bands for our retrievals, the large bias that still exists at those two wavelengths remains an assumption based on the selected aerosol optical model rather than an AOD retrieval result. For the actual AOD retrievals, the RMSE of the aggregate data is shown in Table 3; compared to Fig. 4, the AOD discrepancies change by -9 , -6 , -2 , and $+3$ % for the blue, green, red, and NIR bands due to the surface model refinements. The statistics of the AOD and also the ANG retrievals for the surface model adjustment are shown in Table 3. Note that we also ran the algorithm with the blue and green bands included, but the results were very poor because of sensitivity to poorly constrained scene characteristics, as mentioned in Sect. 2.1 above. We tried running the algorithm with just the green, red, and NIR as well, but the AOD results were still not as good as just using the red and NIR.

3.3 Aerosol components and mixtures

The Version 22 MISR SA aerosol type retrievals have been assessed in light of aerosol particle properties measured during field campaigns (e.g., Kahn et al., 2009c; Patadia et al., 2013) and aggregated from surface network observations (Kahn et al., 2010; Kahn and Gaitley, 2014). Components and mixtures considered in the RA climatology are informed by these results, as well as by additional sensitivity analysis summarized here.

3.3.1 Real part of refractive index

Particle property retrievals are multi-dimensional, and early sensitivity studies showed no ability to constrain the real part of the refractive index (n_r) from MISR data alone, due to uncertainties in the retrieved values of better-constrained variables (Kahn et al., 1998; Chen et al., 2008). As such, the MISR SA Version 22 (and previous versions) arbitrarily assumed a fixed value of n_r for all spherical particles of 1.45. However, despite low retrieval sensitivity, the selected value of n_r affects the retrieved AOD. Specifically, an over-estimated n_r in the retrieved particle type compared to the actual atmosphere, with other factors fixed, produces a systematically reduced value of retrieved AOD. Essentially, as

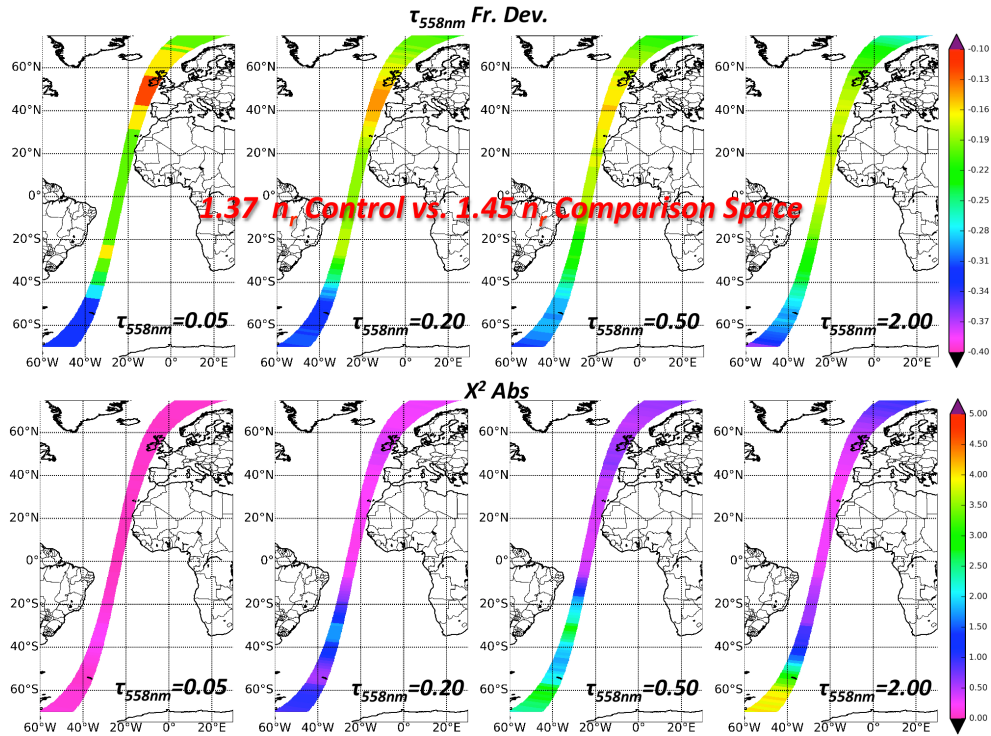


Figure 6. Real part of refractive index sensitivity study. The top four panels show the fractional change in retrieved AOD for an atmosphere containing 1.28 micron non-absorbing particles with $n_r = 1.37$, when the comparison space contains the same size particles but with $n_r = 1.45$, for 558 nm AOD values of 0.05, 0.20, 0.50, and 2.0. The bottom four panels present the χ^2_{abs} values for the lowest residual retrieved AOD for the same four AOD values. As values vary with retrieval geometry, results are plotted for an illustrative orbit, orbit 70499, 20 March 2013. Over-water conditions are assumed everywhere, with the surface pressure prescribed as 1013.25 mb, and the surface wind speed set to 2.5 m s^{-1} . A more extensive analysis of n_r sensitivity, covering a range of particle sizes, is given in the Supplement.

Table 4. MISR components for the 774-mixture set*.

Component name	r_1 (μm)	r_2 (μm)	r_e (μm)	σ	$E(\text{B/G})$	$E(\text{R/G})$	$E(\text{NIR/G})$	$n_r(\text{G})$	SSA(B)	SSA(G)	SSA(R)	SSA(NIR)	$g(\text{G})$
sph_nonabs_0.06	0.002	0.329	0.056	1.650	1.947	0.548	0.226	1.520	1.000	1.000	1.000	1.000	0.357
sph_nonabs_0.12	0.003	0.747	0.121	1.700	1.512	0.669	0.357	1.500	1.000	1.000	1.000	1.000	0.597
sph_nonabs_0.26	0.005	1.690	0.262	1.750	1.185	0.820	0.576	1.450	1.000	1.000	1.000	1.000	0.717
sph_nonabs_0.57	0.008	3.805	0.568	1.800	0.993	0.972	0.877	1.410	1.000	1.000	1.000	1.000	0.750
sph_nonabs_1.28	0.013	8.884	1.285	1.850	0.956	1.039	1.082	1.370	1.000	1.000	1.000	1.000	0.769
sph_abs_0.12_0.80_flat	0.003	0.747	0.121	1.700	1.461	0.687	0.378	1.500	0.818	0.822	0.825	0.828	0.604
sph_abs_0.12_0.80_steep	0.003	0.747	0.121	1.700	1.453	0.698	0.403	1.500	0.838	0.822	0.801	0.756	0.604
sph_abs_0.12_0.90_flat	0.003	0.747	0.121	1.700	1.488	0.677	0.367	1.500	0.910	0.912	0.913	0.915	0.601
sph_abs_0.12_0.90_steep	0.003	0.747	0.121	1.700	1.484	0.683	0.379	1.500	0.920	0.912	0.900	0.875	0.601
dust_grains_mode1_h1	0.100	1.000	0.754	1.500	0.895	1.065	1.079	1.510	0.920	0.977	0.994	0.997	0.711
spheroidal_mode2_h1	0.100	6.000	2.400	2.000	0.989	1.019	1.050	1.510	0.810	0.902	0.971	0.983	0.772
baum_cirrus_De=10um	2.000	9500.000	5.000	n/a	1.000	1.000	1.000	1.317	1.000	1.000	1.000	1.000	0.787
baum_cirrus_De=40um	2.000	9500.000	20.000	n/a	1.000	1.000	1.000	1.317	1.000	1.000	1.000	1.000	0.810
baum_cirrus_De=100um	2.000	9500.000	50.000	n/a	1.000	1.000	1.000	1.317	1.000	1.000	1.000	1.000	0.869

* r_1 , r_2 are the upper and lower limits of the component particle size distribution; r_e is effective radius (μm), σ is the log-normal size distribution width, E is the spectral ratio of extinction cross-section, g is the asymmetry parameter; dust grain and spheroid optical properties from Kalashnikova et al. (2005); cirrus from Baum et al. (2005).

n_r increases, other things being equal, the curvature of the particle single-scattering phase function $P(\theta)$ (where θ is the scattering angle) increases, directing a larger fraction of scattered light into the backward directions where MISR observes. So as n_r increases, less AOD is required to match the observed reflectance, producing lower retrieved AOD. For

larger sea-salt particles in particular, n_r is typically around 1.37, closer to the value for pure water (1.33) than to 1.45 (e.g., Dubovik et al., 2002; Smirnov et al., 2003). Here we adopt n_r of 1.37 for the 1.28 and 2.80 micron effective radius (r_e) spherical sea-salt and other hydrated aerosol optical analogs in a 774-mixture RA particle climatology. We use

Table 5. Mixing groups comprising the 774-mixture set.

Component 1	Component 2	Component 3
spherical_nonabsorbing_0.06	spherical_nonabsorbing_1.28	spherical_nonabsorbing_0.57
spherical_nonabsorbing_0.12	spherical_nonabsorbing_1.28	spherical_nonabsorbing_0.57
spherical_nonabsorbing_0.26	spherical_nonabsorbing_1.28	spherical_nonabsorbing_0.57
spherical_nonabsorbing_0.06	dust_grains_mode1_h1	spheroidal_mode2_h1
spherical_nonabsorbing_0.12	dust_grains_mode1_h1	spheroidal_mode2_h1
spherical_nonabsorbing_0.26	dust_grains_mode1_h1	spheroidal_mode2_h1
spherical_nonabsorbing_0.06	spherical_nonabsorbing_1.28	dust_grains_mode1_h1
spherical_nonabsorbing_0.12	spherical_nonabsorbing_1.28	dust_grains_mode1_h1
spherical_nonabsorbing_0.26	spherical_nonabsorbing_1.28	dust_grains_mode1_h1
spherical_absorbing_0.12_0.80_steep	spherical_nonabsorbing_1.28	dust_grains_mode1_h1
spherical_absorbing_0.12_0.80_flat	spherical_nonabsorbing_1.28	dust_grains_mode1_h1
spherical_absorbing_0.12_0.90_steep	spherical_nonabsorbing_1.28	dust_grains_mode1_h1
spherical_absorbing_0.12_0.90_flat	spherical_nonabsorbing_1.28	dust_grains_mode1_h1
baum_cirrus_De=10um	–	–
baum_cirrus_De=40um	–	–
baum_cirrus_De=100um	–	–

this larger climatology as an alternative to the 74-mixture set from the V22 MISR SA that was applied in the baseline case; Table 4 lists the alternative components and their key optical properties, and Table 5 summarizes the mixtures included in the validation section experiments. Figure 6 demonstrates how overestimating the real part of the refractive index can lead to retrieved-AOD underestimation for a spherical particle size distribution having effective radius 1.28 microns. The top four plots in Fig. 6 show the retrieved AOD fractional error when the simulated atmosphere contains 1.28 micron non-absorbing particles with $n_r = 1.37$, and the comparison space contains 1.28 micron non-absorbing particles but with $n_r = 1.45$, for a range of observational geometries and AOD values (a fractional error of -0.2 indicates underestimation by 20%). Note that overestimating n_r can lead to large negative biases regardless of the absolute AOD. In the case of our 1.28 micron coarse-mode particle, the change from $n_r = 1.45$ to 1.37 results in a $\sim 25\%$ increase in retrieved AOD. The second row in Fig. 6 illustrates how little sensitivity the retrieval has to n_r ; although the fractional deviations are high, the absolute χ^2 values are low (generally < 1.0), highlighting the need for the assumed n_r values to be as close to the natural values as possible. Overall, the sensitivity of retrieved AOD to the value of n_r assumed in the climatology tends to peak for particles having r_e between about 0.25 and 1.3 microns for most MISR observing geometries, based on additional sensitivity analysis. The Supplement contains an analysis of retrieved AOD error similar to the top row of Fig. 6, for a range of particle sizes, and with n_r values as well as AOD varying systematically for the particle assumed in the algorithm comparison space.

3.3.2 Component particle optical analogs, mixtures, and mixing rules

Following Kahn et al. (2010), we add to the RA climatology spherical aerosol components having r_e of 0.57 and 1.28 microns, representing medium and coarse-mode spherical particles. We also add cirrus optical analogs (Pierce et al., 2010), smoke and pollution analogs having spectrally steep and flat particle absorption, respectively (Chen et al., 2008), and mixtures containing both dust and smoke analogs. These represent aerosol types present in the atmosphere but lacking from the V22 SA climatology. The components used for the current analysis are summarized in Table 4.

Taking all combinations of components 1, 2, and 3 in Table 5, in increments of 10 % green-band AOD contribution, with repeated mixtures removed, creates most of the aerosol mixtures used for this study. In addition, we allow the lowest non-zero contribution of each component particle to be 5 %, and adjust the other components accordingly. When cirrus particles are considered, they are not mixed with other species in the column, as this would require including aerosol layers at different elevations in the radiative transfer code, which is beyond our current capabilities. Because there are fewer operational demands on the RA than on the SA, we can afford to characterize aerosol mixtures optically by creating layer-effective phase functions from the components in the mixture before running the radiative transfer code, according to the following:

$$P_{\text{mix}}(\Theta, \lambda) = \sum_n P_n(\Theta, \lambda) \cdot f_n(\lambda) \cdot \text{SSA}_n(\lambda). \quad (3)$$

SSA_n is the spectral single-scattering albedo of component n of the mixture, representing the scattered fraction of

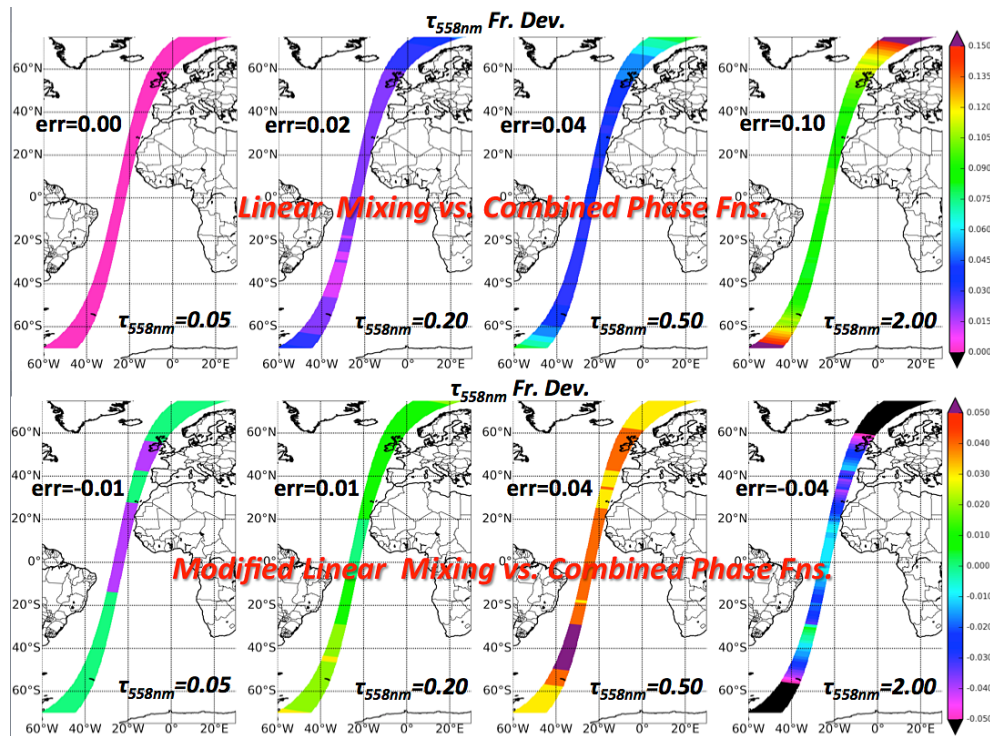


Figure 7. Modified linear mixing (MLM) sensitivity study, showing the fractional change in retrieved AOD for a two-aerosol-component atmosphere containing spherical particles having $r_e = 1.28$ and 0.06 micron, 50 % mid-visible AOD each. The top four panels show the fractional retrieved-AOD change when both components are non-absorbing and a linear mixing approximation is used to combine the particles rather than creating layer-effective phase functions according to Eq. (3). The bottom four panels show the fractional change in retrieved AOD when the MLM approximation is used to combine a 1.28 micron non-absorbing particle with a 0.06 micron absorbing particle, having $SSA = 0.80$ at a wavelength of 558 nm, rather than using layer-effective phase functions. For both sets of panels, the total-column AOD values at 558 nm are 0.05 , 0.20 , 0.50 , and 2.0 , progressing from left to right. The orbit-mean AOD error (err) is indicated in each panel. As values vary with retrieval geometry, these forward model results are plotted for an illustrative orbit, orbit 70499, 20 March 2013. Over-water conditions are assumed everywhere, with the surface pressure prescribed as 1013.25 mb, and the surface wind speed set to 2.5 m s $^{-1}$. A more extensive analysis of the impact of linear mixing and MLM on retrieved AOD is given in the Supplement.

light extinction by that component, P is the particle spectral single-scattering phase function, f_n is the spectral fractional AOD contribution of the particle at wavelength (λ), and Θ is the scattering angle. $P_{\text{mix}}(\Theta, \lambda)$ is normalized by fitting a 5th order spline in $\cos(\Theta)$ space to $P_{\text{mix}}(\Theta, \lambda)$, integrating the spline from -1 to 1 and scaling $P_{\text{mix}}(\Theta, \lambda)$ to 2 . The spectral extinction and SSA for the components in the layer are combined similarly (e.g., Diner et al., 2008). This avoids the assumptions involved in the modified linear mixing (MLM) approach employed in the standard algorithm (Abdou et al., 1997), which can cause substantial high AOD biases, especially when components having significantly different sizes or SSA values are mixed at high AOD. Figure 7 illustrates the situation for a two-particle mixture; orbit-average retrieved-AOD differences can be as large as 10 % for the cases shown, and the differences depend on observing geometry, as well as both the size and SSA differences between the two components. The major cost of eliminating MLM is the size required for the look-up tables (LUTs). For 774 mixtures, the LUT is ~ 8 GB in size. The statistics

of the AOD and ANG retrievals for the 774-mixture set are shown in Table 3. It is clear from Table 3 that the addition of the 774 mixtures results in improved AOD retrievals in both the blue and green, as well as significantly improved ANG retrievals. The Supplement provides a more complete analysis of the impact linear mixing and modified linear mixing have on retrieved AOD, compared to retrievals using layer-effective phase functions (Eq. 3), covering a broad range of the particle relative sizes, mixing proportions, and SSA values.

3.4 Spectral measurement uncertainty estimation

Following the SA, we previously set the reflectance measurement uncertainty estimates for the χ^2 test variables (e.g., ρ_{err} in Eq. 1) equal to 5 % of the reflectance value or 0.002 , whichever is larger. Here we estimate the actual spectral reflectance measurement uncertainty separately for each camera and spectral band, making use of the validation data sets and the aggregate of adjustments and corrections de-

scribed above, as well as a calibration adjustment discussed in Sect. 4.1, with the following uncertainty metric:

$$\varepsilon(\lambda, c) = \frac{\sum_{\text{mix}} \frac{|\rho - \rho_{\text{mod}}|}{\rho}}{n_{\text{mix}}} \quad (4)$$

Here $\rho(\lambda, c)$ is the TOA reflectance observed by MISR for camera (c) and band (λ), and ρ_{mod} is the corresponding value calculated with the forward radiative transfer code for each mixture that passes the χ^2_{abs} acceptance criterion, using the AERONET/MAN spectral AOD values as constraints, and the sum is performed over all passing mixtures (Fig. 1, middle branch).

Figure 8 shows the median (dots) and whiskers give the 25th–75th percentile values. We provide 68th percentile values (bottom of the figure, amounting to 1 standard deviation for a Gaussian distribution) of the camera and band-specific aggregated reflectance uncertainty metric (Eq. 4) when all validation cases are considered. These uncertainty values include any error due to uncertainty in the optical modeling (i.e., representations of particle scattering, absorption, and vertical distribution, scene polarization, the ocean surface, etc.), any error due to uncertainty in the MISR radiometric calibration, as well as discrepancies caused by error inherent in the MAN/AERONET data. It is important to note that even though the relative error is quite large for the red and NIR bands, reflectance in these bands is small, and the median absolute error, $|\rho - \rho_{\text{mod}}|$, is only ~ 0.003 for these bands (< 0.002 for NIR in the nadir camera), compared to 0.004 for the green, and ~ 0.01 for the blue, averaged over all nine cameras (plot not shown). Because ρ_{err} should only include MISR model/measurement uncertainty, these plots provide a crude upper bound on the desired quantity. Based on this analysis, we alternatively set ρ_{err} for the χ^2 tests equal to $\max[0.01, \rho]$ multiplied by 0.05, 0.04, 0.055, 0.08, for blue, green, red and NIR bands. Note that the forward modeling errors for the blue and green bands over dark water could be significant, so the reflectance uncertainties for these bands would need to be reassessed for over-land retrievals. We find that applying this minimum uncertainty formulation gives more appropriate relative weight to the NIR band in the total χ^2 calculation over water, i.e., generally a smaller denominator and therefore greater weight at low AOD, and lower weight at high AOD. These changes also result in the loss of $< 1\%$ of 3×3 retrieval regions used in the analysis because small deviations in the NIR at low AOD result in high χ^2 values. The factors calculated here apply to dark water surfaces; multipliers would have to be derived from appropriate validation cases for other surface types.

4 Algorithm empirical adjustments and validation

In this section we assess the cumulative effect of the algorithm modifications based on physical considerations described in Sect. 3. But in addition to these modifications, our

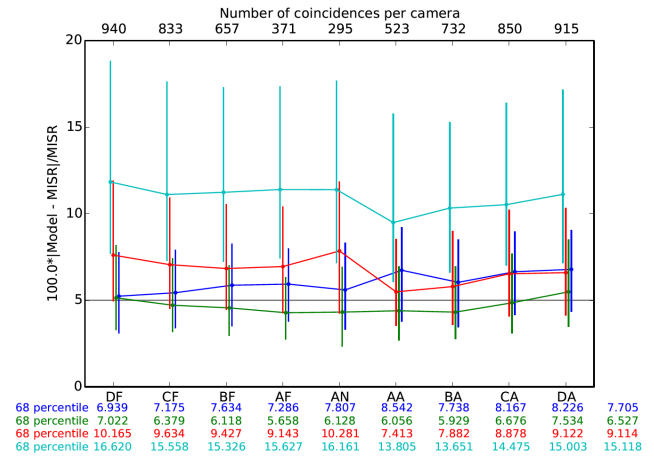


Figure 8. Total percent retrieval error in TOA reflectance assessed relative to the corresponding AODs from the AERONET/MAN validation data set (Eq. 4). Unlike Figs. 3 and 5, the 68th percentile values for each camera and band are given along the bottom of the plot, and the band-average values are shown in the rightmost column.

validation data allow us to make some empirical adjustments to factors in the algorithm for which existing physical constraints are loose. This includes the stringency with which we apply cloud screening, and band-to-band calibration within the $\sim 1.5\%$ accuracy to which it is determined by formal instrument calibrations procedures (Bruegge et al., 2007).

4.1 Calibration adjustments based on Ångström exponent comparisons

Figure 9a and b show a large (~ 0.15 – 0.20) negative bias in the retrieved ANG compared to the validation data for $\text{AOD} > 0.20$, even though all the spectral adjustments to the retrieval assumptions have been made (excluding the reflectance uncertainty adjustments of Sect. 3.4). This leaves adjustments to the relative radiometric calibration ($< 1\%$) in the red and NIR bands as possible corrections, given the great sensitivity of ANG to small changes in these quantities. We find that increasing the MISR red band radiances by 0.75% and lowering the NIR band radiances by 0.75% results in a substantially lower-magnitude bias in the retrieved ANG for both MISR-MAN coincidences and MISR-AERONET coincidences. This adjustment causes the ANG RMSE to decrease by more than 20% for both data sets at high AOD (> 0.20), results in an ANG bias that is less than 0.10 in magnitude, and leaves the AOD validation statistics essentially unchanged. Panels c and d show improved ANG slopes when the χ^2 criterion used incorporates the reflectance uncertainty adjustment described in Sect. 3.4. Any further adjustment to the radiometric calibration would create greater positive bias in ANG for some of the low AOD bins (Fig. 10b). Although we find that modifying the calibration of the red and NIR bands can bring the ANG retrievals

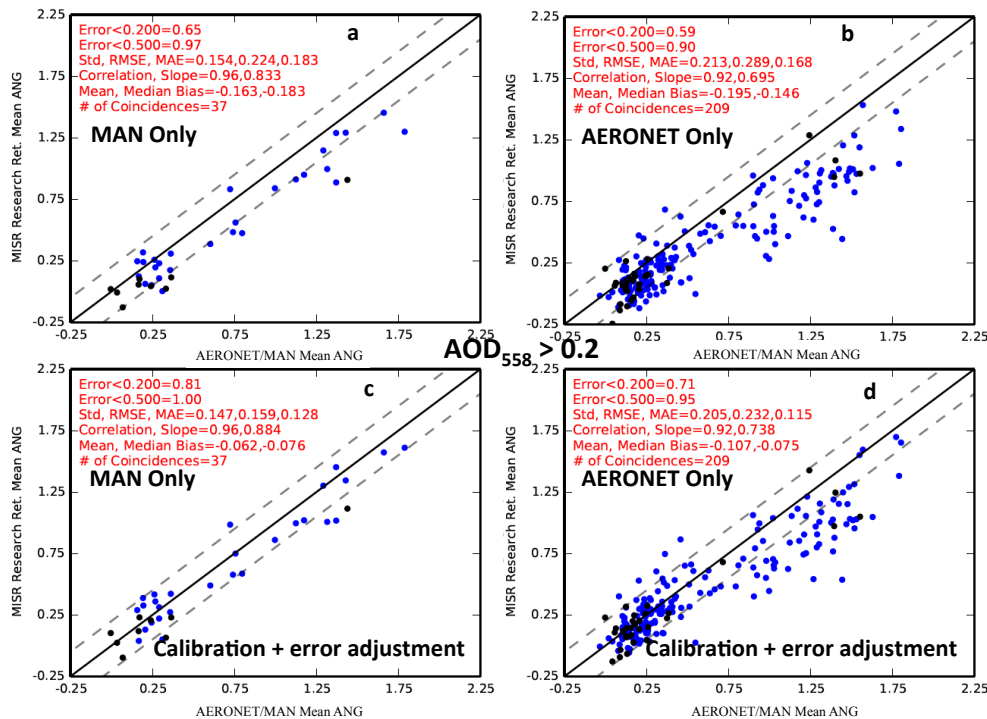


Figure 9. Scatter-plots showing MISR vs. AERONET/MAN ANG data for AOD > 0.20, with all modifications (c, d), and with all modifications except the calibration corrections and the error adjustment (a, b). The MISR-MAN coincidences are given in panels (a) and (c), and the MISR-AERONET coincidences correspond to panels (b) and (d). Blue dots represent coincidences with a MAN/AERONET 558 nm AOD of between 0.2 and 0.5. Black dots represent coincidences with AERONET/MAN AOD values > 0.5. Statistics for the ANG plots are presented in Table 3.

into better alignment with AERONET/MAN without affecting the AOD statistics, we are not drawing any conclusions about the radiometric calibration of MISR itself. Other factors, such as particle-model errors, surface-representation errors, uncorrected scene polarization, and more subtle aspects of the radiometric calibration could contribute to biases in RA-retrieved ANG.

4.2 Ångström Exponent validation and adaptive χ^2 selection criterion

ANG validation against AERONET/MAN is shown in Fig. 10a. The second line in each triplet series of whiskers (SA, RA-baseline, RA-modified) was generated with the traditional $\min(\chi_{\text{abs}}^2) \cdot 1.5$ mixture acceptance metric used previously, whereas the third whisker was created using a different criterion involving χ_{abs}^2 . This alternative criterion is $\min(\chi_{\text{abs}}^2) + 0.35$ for AOD = 0.0 and $\min(\chi_{\text{abs}}^2) \cdot 1.5$ for AOD ≥ 0.20 , with a linearly weighted value for AODs between 0.0 and 0.20. This results in 68th percentile errors (for the seven lowest AOD bins) that are $\sim 10\%$ lower than the standard $\min(\chi_{\text{abs}}^2) \cdot 1.5$. We use this adaptive χ^2 criterion for the remainder of the paper because the AODs are not negatively affected, and the use of an absolute criterion makes sense at low AOD due to the limits of measurement sensi-

tivity to particle properties in this regime (e.g., Kahn et al., 2011).

Figure 10a and Table 3 show that the MISR RA sensitivity to ANG improves dramatically as AOD increases, as expected (Kahn et al., 2010; Kahn and Gaitley, 2014), with 68th percentile values of ANG statistical discrepancy dropping from 0.51 at an AOD of < 0.04 down to ~ 0.25 for AODs between 0.08–0.095. ANG sensitivity continues to improve as AOD increases, with 68th percentile errors dropping further, to ~ 0.17 , for AOD > 0.35. Correlation and slope also improve with increasing AOD (see Fig. 9c and d). Figure 10b shows a scatter plot of MISR RA ANG (computed using the mean spectral extinction cross-section ratios over all passing mixtures) vs. AERONET/MAN ANG for all AOD > 0.01. Overall, 67% of the MISR RA ANG values fall within 0.275 of the MAN/AERONET ANG value.

Figures 10a (left whisker in triplet) and c (also Table 3) show ANG, calculated from the SA AOD retrievals, compared to AERONET/MAN. We computed these ANGs from the SA-retrieved best-estimate spectral AODs, which represent the mean spectral AOD of all passing mixtures. This makes our definition of ANG (for the SA) identical to the one for the SA “best-estimate ANG” (Bull et al., 2011). We use the extinction cross-section ratios averaged over all passing mixtures to compute ANG for the RA rather than the

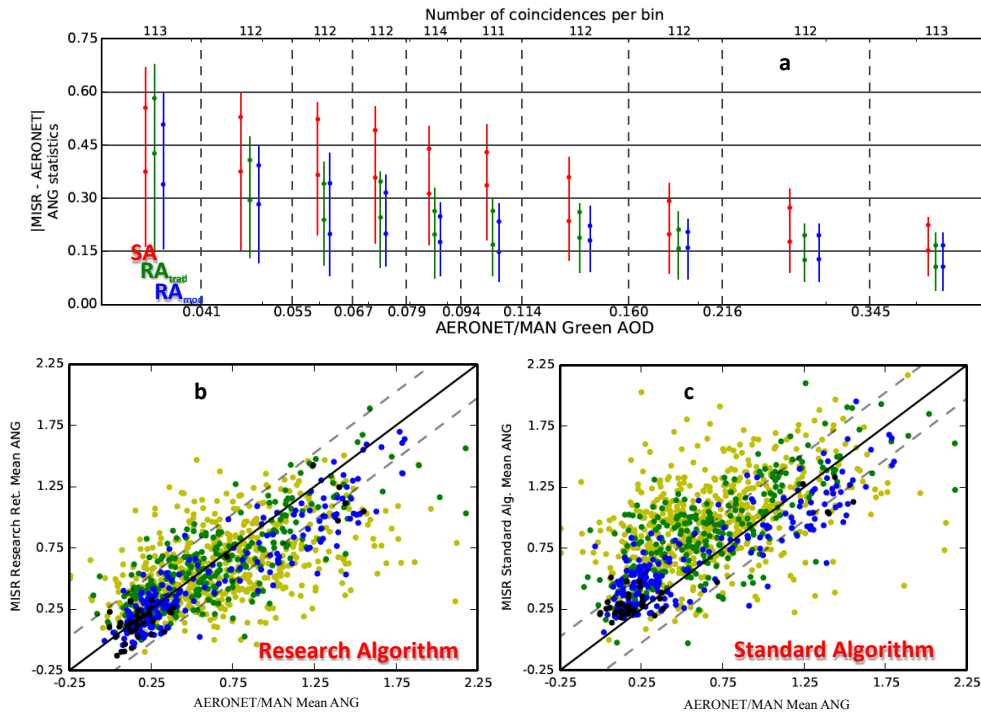


Figure 10. Panel (a) shows the statistics of the $[\text{MISR-MAN}/\text{AERONET}]$ Ångström Exponent coincidences, conditioned on 558 nm AERONET/MAN AOD. The first line of the triplets shows the SA-AERONET/MAN comparison, the second line shows the comparison between the RA and MISR-MAN/AERONET with the standard χ^2_{abs} criterion applied, and the 3rd line shows the comparison between the RA and MISR-MAN/AERONET with the modified χ^2_{abs} criterion. The vertical lines represent the 25th–75th percentiles, the lower dot represents the median absolute error and the upper dot represents the 68th percentile value. The number of coincidences per AOD bin is listed at the top of the plot. The upper limit of each green-band AOD bin (binning is done based on green band AOD) is shown at the bottom (except for the last AOD bin, which includes all higher AOD cases). Panels (b) and (c) show the MISR-AERONET/MAN ANG cases for all AOD > 0.01, for the research algorithm (all modifications with updated χ^2_{abs} criterion) and standard algorithm, respectively. Yellow dots correspond to points with AERONET AOD less than 0.10, green dots represent AOD between 0.10 and 0.20, blue dots indicate AOD between 0.20 and 0.50, and black dots designate AOD values greater than 0.50. Statistics for the ANG plots are presented in Table 3.

spectral AODs, because we allow the RA to select 0.0 for the minimum AOD, which would otherwise complicate the ANG calculation. Compared to the SA, there is 36 % improvement in the median-absolute-error overall, the RMSE drops by 17 %, the correlation coefficient increases by 0.06, and the median bias is much lower in magnitude for all AODs. The slope of the regression line improves by ~ 0.10 for AOD > 0.22 (not shown), but the RA slope is ~ 0.03 lower than the SA for AOD < 0.10. Before modifying the χ^2 acceptance criterion, the SA-retrieved ANG more closely matched AERONET/MAN ANG values at low AOD, possibly owing to the fact that only 74 aerosol mixtures are employed, vs. the 774 used for the RA. Because the RA is likely not sensitive to differences among all these mixtures at low AOD, increasing the number of mixtures selected (which is what occurs at low AOD with the larger mixture climatology and χ^2 criterion modification) tends to reduce outliers, increase the correlation, and decrease the slope. As AOD approaches 0.20, the impact of this modification diminishes, and the greater variety of aerosol models allows for a more robust ANG re-

trieval. It is likely that external constraints are needed to winnow down the passing-mixture list at low AOD, such as using an aerosol transport model to select among the list of passing mixtures (e.g., Kahn, 2012; Li et al., 2014), as the information content of the MISR radiances tends to be swamped by surface effects and Rayleigh scattering signals under these circumstances.

4.3 AOD validation

Figures 11 and Table 3 show the aggregated effects of the median-or-min reflectance selection approach, under-light + updated whitecaps, updated n_r , new mixtures, layer-effective single-scattering phase function, and the calibration adjustment, as well as the effect of using the modified χ^2_{abs} metric described in Sect. 4.2. Taken together, the aggregated changes compare favorably relative to the RA baseline case, as shown in Table 3, with RMSE decreases of 27, 20, 14, and 8 % for blue, green, red, and NIR, respectively. For the RA over dark water, 62, 68, 72, and 74 % of retrievals fall within

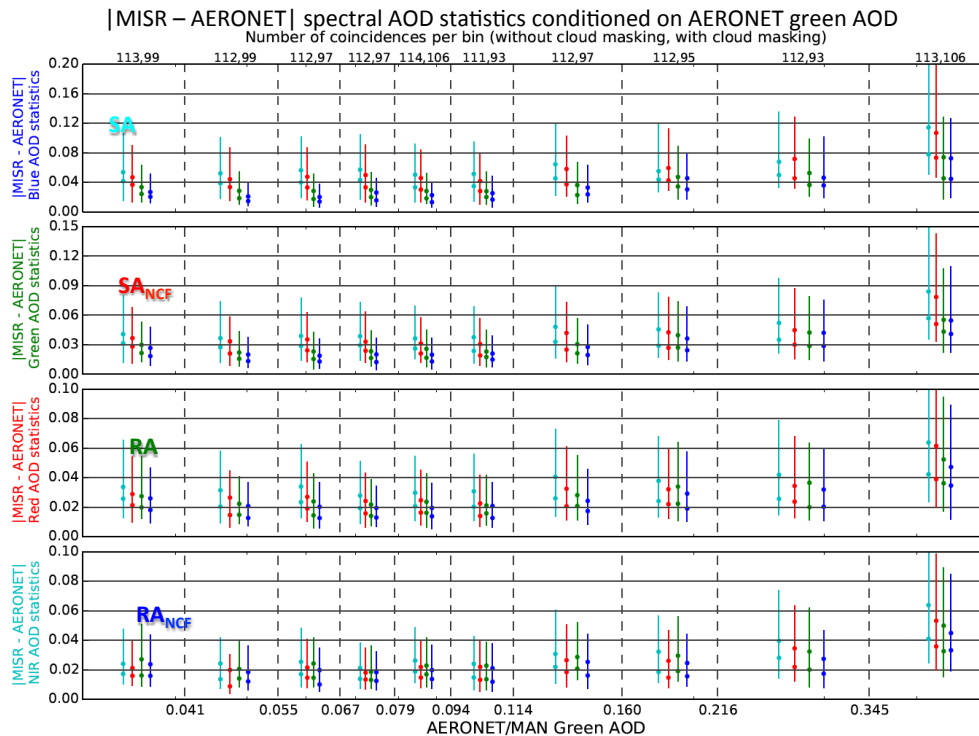


Figure 11. $|MISR - AERONET|$ spectral AOD statistics conditioned on AERONET green AOD. For the vertical lines and points: cyan represents the SA, red represents the SA with enhanced cloud screening ($FNC < 0.50$), green represents the RA with all modifications through Sect. 4.2, and blue represents the RA with all modifications and enhanced cloud screening ($FNC < 0.50$). The vertical lines indicate the 25th–75th percentiles, and the lower dot gives the median absolute error. The upper dot represents the 68th percentile value. Each row of plots presents results for one of the four MISR spectral bands (blue, green, red, and NIR). The number of coincidences per AOD bin is listed at the top of the plot (without, and then with enhanced cloud masking). Vertical dashed lines separate AOD bins, which are defined based on the green band AOD. The upper limit of each (green band) AOD bin is shown at the bottom (except for the last AOD bin, which includes all higher AOD cases).

the greater of 0.03 or 10 % of the validation AOD values in the blue, green, red, and NIR bands.

Table 3 also gives the results of the MISR SA AOD for the same sites and same retrieval regions used for the RA. Compared to the SA, the upgraded RA RMSE drops by 36, 29, 21 and 12 % in the blue, green, red, and NIR bands. The fraction of AOD retrievals falling within the greater of 0.03 or 10 % of the validation AOD values changes by +0.24, +0.16, +0.09 and +0.04. The correlation (r) between the SA and AERONET/MAN is ≥ 0.94 at all wavelengths, and is ≥ 0.96 for the RA.

Figure 11 shows the error statistics of $|MISR - AERONET/MAN|$ spectral AOD for different AOD regimes. This figure demonstrates that the upgraded RA performs better than the SA over most AOD bins (and wavelengths). The largest improvements are seen at both very low AOD (< 0.10) and at higher AOD ($> \sim 0.35$), as well as at shorter wavelengths.

4.4 Enhanced cloud screening

Figure 11 and Table 3 also show the effect of applying a maximum FNC of 0.50 to the RA with all adjustments described above applied, and to the SA. This is similar to the approach taken by Witek et al. (2013), except that we do not consider glint-contaminated cameras in the FNC count. Note that our application removes an additional 13 % of 3×3 retrieval regions (as compared to a much higher fraction for Witek et al., 2013). However, the 0.01 AOD bias that was present at all wavelengths is now reduced to ~ 0.005 for all wavelengths. Every statistic except slope improves when the FNC limit is applied (Table 3). The standard algorithm AOD retrieval sees a greater improvement than the research algorithm with this adjustment, which is likely due to the SA having poorer statistics overall to begin with. Interestingly, setting the FNC to 0.50 had virtually no effect on the retrieved ANG statistics (RMSE, MAE), except for the slope, which increased from 0.471 to 0.511, likely due to preferential removal of larger cloud droplet and/or larger, hydrated particle contributions.

This also occurs for the SA, with the slope increasing from 0.493 to 0.521.

Shi et al. (2014) used MODIS cloud-detection products that make use of spectral channels at longer wavelengths than those available on MISR to screen for clouds in coincident MISR aerosol retrievals. They identify a probable thin cirrus contribution averaging about 0.01 to the AOD retrievals over ocean, and larger effects in the vicinity of cloud edges. It is beyond the scope of the current paper to include MODIS cloud masking, but overall, the implementation of a maximum fraction not-clear even within the MISR products alone results in a large improvement to the standard algorithm (as also shown by Witek et al., 2013), and a more modest improvement to the research algorithm results. The MISR cloud-contamination issue warrants further study, as does the possible use of MODIS infrared channels to refine the cloud screening.

5 Conclusions

In this paper, we assess the impacts of changes to the MISR research aerosol retrieval algorithm over water, modifications based on physical considerations, as well as empirical adjustments that improve comparisons with validation data and fall within the range of allowed values based on all other available constraints. In the process, we assess the impact on retrieved AOD of several assumptions commonly employed in aerosol remote sensing, and some assumptions that are specific to the MISR standard algorithm. We accomplish this by systematically altering the algorithm such that each modification is performed independently, and the results are compared against more than 1100 MAN-AERONET coincident, dark-water observations (Table 3).

We show that the cumulative effect of several physically motivated changes eliminates about half the statistical bias in the retrieved AOD. Specifically, (1) the small increase in TOA model reflectance in the red band produced by including spectral under-light contributions causes the retrieved red band AOD to drop relative to the NIR, resulting in the algorithm systematically selecting larger particles. The consequent reduction in ANG reduces the retrieved mid-visible AOD bias and improves the ANG correlation. (2) Correcting the n_r value assumed for hydrated particle optical models can increase retrieved AOD at all AOD values, by up to 25 % if the retrieved particle is large. (3) Removing the linear mixing approximation reduces AOD overestimation at all AODs, but especially at higher AOD. (4) An adaptive pixel selection technique is introduced that minimizes the effects of unmasked cloud at low AOD, and of aerosol variability at high AOD. For the RA, this change causes spectral AOD RMSE to decrease by 5–10 %. And (5), in Sect. 3.3.2, we show the impact of including a greatly expanded mixture list; this causes the AOD RMSE to change by –16 to +5 %, with the only increase occurring in the NIR, where the statistics were already

much better than the other bands before this adjustment was applied.

All modifications are then aggregated and an error analysis is performed to produce an empirical estimate of the reflectance uncertainty, used for the χ^2 calculations. A spectrally invariant uncertainty of 5 % was previously assumed for both the MISR standard and research algorithms. However, the relative uncertainty is much higher in the NIR than the red band, which is especially important for over-water retrievals. In addition, the minimum value used for the χ^2 uncertainty was too large for the NIR, which caused less weighting to be assigned to the NIR band than was appropriate at low AOD. After making all corrections, small empirical calibration adjustments of +0.75 and –0.75 % were applied to red and NIR bands, respectively, to bring ANG into substantially better agreement with AERONET without significantly affecting AOD performance.

Applying all these physically based and empirical adjustments decreased AOD RMSE by 8–27 % compared to the algorithm before any corrections were implemented, and an RMSE decrease of 12–36 % compared to the SA. ANG RMSE dropped by 17 % compared to the SA, and MAE decreased 36 %. Enhanced cloud-screening, implemented by setting a fraction not-clear maximum of 50 %, brought the spectral AOD bias to ~ 0.005 , and greatly reduced the number of outliers, while only removing 13 % of 3×3 retrieval regions.

These results make clear that adding a relatively simple under-light model, modifying particle properties to be more realistic, introducing a comprehensive mixture list, (in the case of the research algorithm) making a small calibration correction, and implementing an enhanced cloud mask can dramatically improve the aerosol retrievals.

Other factors that remain to be considered include: (1) the angular dependence of ocean surface reflectance (BRDF), (2) the coupled impact of polarization and uncertain aerosol vertical distribution on the retrieved quantities, which could be significant for over-ocean transported aerosol residing in the free troposphere, (3) the use of an aerosol transport model or other external source to constrain aerosol type when many mixtures pass the algorithm acceptance criteria, e.g., frequently at low AOD, (4) the use of coincident MODIS infrared spectral bands to help with cloud-screening, and (5) further examination of the MISR radiometric calibration. However, at least based on the 1129 over-ocean validation cases included here, the adjustments applied are sufficient to remove nearly all the apparent bias in both AOD and ANG.

The updated MISR RA (with all of the corrections made) will continue to serve as our platform for testing retrieval ideas, and for extracting the maximum particle-type information on a case-by-case basis for local and regional-scale studies. However, for the community to take advantage of these improvements for global-scale applications, the adjustments demonstrated here must be implemented in an opera-

tional code that can run efficiently on large volumes of MISR data, a non-trivial task in itself.

The Supplement related to this article is available online at doi:10.5194/amt-7-3989-2014-supplement.

Acknowledgements. We thank our colleagues on the Jet Propulsion Laboratory's MISR instrument team and at the NASA Langley Research Center's Atmospheric Sciences Data Center for their roles in producing the MISR data sets, and our colleagues at the NASA Goddard Space Flight Center, the SeaWiFS, MERIS, and MODIS ocean color teams, the ESA, the GlobColour group, Brent Holben and the AERONET team, and Alexander Smirnov and the MAN team for the invaluable data sets they produce. We also thank Sergey Korokin, Alexei Lyapustin, Leigh Munchak, Falguni Patadia, and Andrew Sayer for helpful discussions, Jeff Reid and Andrew Sayer for thorough and constructive reviews, and Maksym Petrenko for identifying the MISR/MAN coincidences. This research is supported in part by NASA's Climate and Radiation Research and Analysis Program under H. Maring, NASA's Atmospheric Composition Program under R. Eckman, and the NASA Earth Observing System MISR instrument project.

Edited by: A. Kokhanovsky

References

- Abdou, W. A., Martonchik, J. V., Kahn, R. A., West, R. A., and Diner, D. J.: A modified linear-mixing method for calculating atmospheric path radiances of aerosol mixtures, *J. Geophys. Res.*, 102, 16883–16888, doi:10.1029/96JD03434, 1997.
- Antoine, D., Morel, A., Leymarie, E., Houyou, A., Gentili, B., Victor, S., Buis, J.-P., Buis, N., Meunier, S., Canini, M., Crozel, D., Fougne, B., and Henry, P.: Underwater Radiance Distributions Measured with Miniaturized Multispectral Radiance Cameras, *J. Atmos. Ocean. Tech.*, 30, 74–95, 2013.
- Atlas, R., Hoffman, R. N., Ardizzone, J., Leidner, S. M., Jusem, J. C., Smith, D. K., and Gombos, D.: A cross-calibrated, multiplatform ocean surface wind velocity product for meteorological and oceanographic applications, *B. Am. Meteorol. Soc.*, 92, 157–174, doi:10.1175/2010BAMS2946.1, 2011.
- Barrot, G., Mangin, A., and Pinnock, S.: GlobColour Product User Guide, <http://www.globcolour.info> (last access: 31 January 2014), 2010.
- Baum, B., Yang, P., Heymsfield, A., Platnick, S., King, M., Hu, Y., and Bedka, S.: Bulk scattering properties for the remote sensing of ice clouds: Part II. Narrowband models, *J. Appl. Meteorol.*, 44, 1896–1911, doi:10.1175/JAM2309.1, 2005.
- Bruegge, C. J., Diner, D. J., Kahn, R. A., Chrien, N., Helmlinger, M. C., Gaitley, B. J., and Abdou, W. A.: The MISR radiometric calibration process, *Remote Sens. Environ.*, 107, 2–11, doi:10.1016/j.rse.2006.07.024, 2007.
- Bull, M., Matthews, J., McDonald, D., Menzies, A., Moroney, C., Mueller, K., Paradise, S., and Smyth, M.: MISR Data Products Specifications Revision S, <https://eosweb.larc.nasa.gov/project/misr/dps> (last access: 2 March 2014), 2011.
- Chen, W.-T., Kahn, R. A., Nelson, D., Yau, K., and Seinfeld, J.: Sensitivity of multi-angle imaging to optical and microphysical properties of biomass burning aerosols, *J. Geophys. Res.*, 113, D10203, doi:10.1029/2007JD009414, 2008.
- Diner, D. J., Beckert, J. C., Reilly, T. H., Bruegge, C. J., Conel, J. E., Kahn, R. A., Martonchik, J. V., Ackerman, T. P., Davies, R., Gerstel, S. A. W., Gordon, H. R., Muller, J.-P., Myneni, R., Sellers, R. J., Pinty, B., and Verstraete, M. M.: Multiangle Imaging Spectro-Radiometer (MISR) description and experiment overview, *IEEE T. Geosci. Remote*, 36, 1072–1087, 1998.
- Diner, D. J., Abdou, W. A., Ackerman, T. P., Crean, K., Gordon, H. R., Kahn, R. A., Martonchik, J. V., Paradise, S. R., Pinty, B., Verstraete, M. M., Wang, M., and West, R. A.: Multi-angle Imaging SpectroRadiometer Level 2 Aerosol Retrieval Algorithm Theoretical Basis, Revision G. Jet Propulsion Laboratory, California Institute of Technology JPL D-11400, Pasadena, California, USA, 2008.
- Dubovik, O., Holben, B., Eck, T. F., Smirnov, A., Kaufman, Y. J., King, M. D., Tanre, D., and Slutsker, I.: Variability of Absorption and Optical Properties of Key Aerosol Types Observed in Worldwide Locations, *J. Atmos. Sci.*, 59, 590–608, 2002.
- Frouin, R., Schwindling, M., and Deschamps, P.-Y.: Spectral reflectance of sea foam in the visible and near-infrared: In situ measurements and remote sensing implications, *J. Geophys. Res.*, 101, 14361–14371, doi:10.1029/96JC00629, 1996.
- Holben, B. N., Eck, T. F., Slutsker, I., Tanre, D., Buis, J. P., Setzer, A., Vermote, E., Reagan, J. A., Kaufman, Y. J., Nakajima, T., Lavenu, F., Jankowiak, I., and Smirnov, A.: AERONET – A federated instrument network and data archive for aerosol characterization, *Remote Sens. Environ.*, 66, 1–16, 1998.
- Holben, B. N., Eck, T. F., Slutsker, I., Smirnov, A., Sinyuk, A., Schafer, J., Giles, D., and Dubovik, O.: Aeronet's Version 2.0 quality assurance criteria, *Proc. SPIE 6408, Remote Sensing of the Atmosphere and Clouds*, doi:10.1117/12.706524, 2006.
- Kahn, R. A.: Reducing the uncertainties in direct aerosol radiative forcing, *Surv. Geophys.*, 33, 701–721, doi:10.1007/s10712-011-9153-z, 2012.
- Kahn, R. A. and Gaitley, B. J.: An analysis of global aerosol type as retrieved by MISR, *J. Geophys. Res.*, submitted, 2014.
- Kahn, R. A. and Limbacher, J.: Eyjafjallajökull volcano plume particle-type characterization from space-based multi-angle imaging, *Atmos. Chem. Phys.*, 12, 9459–9477, doi:10.5194/acp-12-9459-2012, 2012.
- Kahn, R. A., Banerjee, P., McDonald, D., and Diner, D.: Sensitivity of Multiangle imaging to Aerosol Optical Depth, and to Pure-Particle Size Distribution and Composition Over Ocean, *J. Geophys. Res.*, 103, 32195–32213, 1998.
- Kahn, R. A., Banerjee, P., and McDonald, D.: The Sensitivity of Multiangle Imaging to Natural Mixtures of Aerosols Over Ocean, *J. Geophys. Res.*, 106, 18219–18238, 2001a.
- Kahn, R. A., Banerjee, P., McDonald, D., and Martonchik, J.: Aerosol properties derived from aircraft multiangle imaging over Monterey Bay, *J. Geophys. Res.*, 106, 11977–11995, 2001b.
- Kahn, R. A., Li, W.-H., Martonchik, J. V., Bruegge, C. J., Diner, D. J., Gaitley, B. J., and Abdou, W.: MISR Calibration and Implications for Low-Light-Level Aerosol Retrieval over Dark Water, *J. Atmos. Sci.*, 62, 1032–1052, 2005a.

- Kahn, R., Gaitley, B., Martonchik, J., Diner, D., Crean, K., and Holben, B.: MISR global aerosol optical depth validation based on two years of coincident AERONET observations, *J. Geophys. Res.*, 110, D10S04, doi:10.1029/2004JD004706, 2005b.
- Kahn, R. A., Garay, M. J., Nelson, D. L., Yau, K. K., Bull, M. A., Gaitley, B. J., Martonchik, J. V., and Levy, R. C.: Satellite-derived aerosol optical depth over dark water from MISR and MODIS: Comparisons with AERONET and implications for climatological studies, *J. Geophys. Res.*, 112, D18205, doi:10.1029/2006JD008175, 2007.
- Kahn, R. A., Martonchik, J. V., Diner, D., Garay, M., Bull, M., and Di Girolamo, L.: MISR Level 2 Aerosol/Surface Products Quality Statement, https://eosweb.larc.nasa.gov/sites/default/files/project/misr/quality_summaries/L2_AS_Products.pdf (last access: 28 August 2014), 2009a.
- Kahn, R. A., Nelson, D. L., Garay, M., Levy, R. C., Bull, M. A., Martonchik, J. V., Diner, D. J., Paradise, S. R., Hansen, E. G., and Remer, L. A.: MISR Aerosol product attributes, and statistical comparison with MODIS, *IEEE T. Geosci. Remote*, 40, 4095–4114, 2009b.
- Kahn, R. A., Petzold, A., Wendisch, M., Bierwirth, E., Dinter, T., Esselborn, M., Fiebig, M., Heese, B., Knippertz, P., Müller, D., Schladitz, A., and von Hoyningen-Huene, W.: Desert Dust Aerosol Air Mass Mapping in the western Sahara, Using particle properties derived from space-based multi-angle imaging, *Tellus*, 61, 239–251, doi:10.1111/j.1600-0889.2008.00398.x, 2009c.
- Kahn, R. A., Gaitley, B. J., Garay, M. J., Diner, D. J., Eck, T., Smirnov, A., and Holben, B. N.: Multiangle Imaging Spectroradiometer global aerosol product assessment by comparison with the Aerosol Robotic Network, *J. Geophys. Res.*, 115, D23209, doi:10.1029/2010JD014601, 2010.
- Kahn, R. A., Garay, M. J., Nelson, D. L., Levy, R. C., Bull, M. A., Diner, D. J., Martonchik, J. V., Hansen, E. G., Remer, L. A., and Tanré, D.: Response to “Toward unified satellite climatology of aerosol properties. 3. MODIS versus MISR versus AERONET”, *J. Quant. Spectrosc. Ra.*, 112, 901–909, doi:10.1016/j.jqsrt.2009.11.003, 2011.
- Kalashnikova, O. V., Kahn, R., Sokolik, I. N., and Li, W.-H.: The ability of multi-angle remote sensing observations to identify and distinguish mineral dust types: Part 1. Optical models and retrievals of optically thick plumes, *J. Geophys. Res.*, 110, D18S14, doi:10.1029/2004JD004550, 2005.
- Koepke, P.: Effective reflectance of oceanic whitecaps, *Appl. Optics*, 23, 1816, doi:10.1364/AO.23.001816, 1984.
- Li, S., Kahn, R., Chin, M., Garay, M. J., Chen, L., and Liu, Y.: Improving satellite retrieved aerosol microphysical properties using GOCART data, *Atmos. Meas. Tech. Discuss.*, 7, 8945–8981, doi:10.5194/amtd-7-8945-2014, 2014.
- Maritorena, S. and Siegel, D. A.: Consistent Merging of Satellite Ocean Color Data Sets Using a Bio-Optical Model, *Remote Sens. Environ.*, 94, 429–440, 2005.
- Maritorena, S., d’Andon, O. H. F., Mangin, A., and Siegel, D. A.: Merged satellite ocean color data products using a bio-optical model: Characteristics, benefits and issues, *Remote Sens. Environ.*, 114, 1791–1804, doi:10.1016/j.rse.2010.04.002, 2010.
- Martonchik, J. V., Diner, D. J., Kahn, R., Verstraete, M. M., Pinty, B., Gordon, H. R., and Ackerman, T. P.: Techniques for the Retrieval of aerosol properties over land and ocean using multiangle imaging, *IEEE T. Geosci. Remote*, 36, 1212–1227, 1998.
- Martonchik, J. V., Diner, D. J., Crean, K., and Bull, M.: Regional aerosol retrieval results from MISR, *IEEE T. Geosci. Remote*, 40, 1520–1531, 2002.
- Monahan, E. C. and O’Muircheartaigh, I. G.: Optimal power-law description of oceanic whitecap coverage dependence on wind speed, *J. Phys. Oceanogr.*, 10, 2094, doi:10.1175/1520-0485(1980)010<2094:OPLDOO>2.0.CO;2, 1980.
- Patadia, F., Kahn, R. A., Limbacher, J. A., Burton, S. P., Ferrare, R. A., Hostetler, C. A., and Hair, J. W.: Aerosol airmass type mapping over the Urban Mexico City region from space-based multi-angle imaging, *Atmos. Chem. Phys.*, 13, 9525–9541, doi:10.5194/acp-13-9525-2013, 2013.
- Pierce, J. R., Kahn, R. A., Davis, M. R., and Comstock, J. M.: Detecting thin cirrus in Multiangle Imaging Spectroradiometer aerosol retrievals, *J. Geophys. Res.*, 115, D08201, doi:10.1029/2009JD013019, 2010.
- Remer, L. A., Kaufman, Y. J., Tanre, D., Mattoo, S., Chu, D. A., Martins, J. V., Li, R.-R., Ichoku, C., Levy, R. C., Kleidman, R. G., Eck, T. F., Vermote, E., and Holben, B. N.: The MODIS aerosol algorithm, products and validation, *J. Atmos. Sci.*, 62, 947–973, doi:10.1175/JAS3385.1, 2005.
- Sayer, A. M., Thomas, G. E., and Grainger, R. G.: A sea surface reflectance model for (A)ATSR, and application to aerosol retrievals, *Atmos. Meas. Tech.*, 3, 813–838, doi:10.5194/amt-3-813-2010, 2010.
- Shi, Y., Zhang, J., Reid, J. S., Liu, B., and Hyer, E. J.: Critical evaluation of cloud contamination in the MISR aerosol products using MODIS cloud mask products, *Atmos. Meas. Tech.*, 7, 1791–1801, doi:10.5194/amt-7-1791-2014, 2014.
- Smirnov, A., Holben, B. N., Eck, T. F., Dubovik, O., and Slutsker, I.: Cloud-Screening and Quality Control Algorithms for the AERONET Database, *Remote Sens. Environ.*, 73, 337–349, doi:10.1016/S0034-4257(00)00109-7, 2000.
- Smirnov, A., Holben, B. N., Dubovik, O., Frouin, R., Eck, T. F., and Slutsker, I.: Maritime component in aerosol optical models derived from Aerosol Robotic Network data, *J. Geophys. Res.*, 108, 4033, doi:10.1029/2002JD002701, 2003.
- Smirnov, A., Holben, B. N., Slutsker, I., Giles, D. M., McClain, C. R., Eck, T. F., Sakerin, S. M., Macke, A., Croot, P., Zibordi, G., Quinn, P. K., Sciare, J., Kinne, S., Harvey, M., Smyth, T. J., Piketh, S., Zielinski, T., Proshutinsky, A., Goes, J. I., Nelson, N. B., Larouche, P., Radionov, V. F., Goloub, P., Krishna Moorthy, K., Matarrese, R., Robertson, E. J., and Jourdin, F.: Maritime Aerosol Network as a component of Aerosol Robotic Network, *J. Geophys. Res.*, 114, D06204, doi:10.1029/2008JD011257, 2009.
- Voss, K. J. and Chapin, A. L.: Upwelling radiance distribution camera system, *NURADS, Opt. Express*, 13, 4250–4262, 2005.
- Witek, M. L., Garay, M. J., Diner, D. J., and Smirnov, A.: Aerosol optical depths over oceans: A view from MISR retrievals and collocated MAN and AERONET in-situ observations, *J. Geophys. Res.*, 118, 12620–12633, doi:10.1002/2013JD020393, 2013.